

Topochemical Modulations from 1D Iron Fluoride Precursor to 3D Frameworks

Arindam Ghosh, Dereje Bekele Tekliye, Emily E. Foley, Varimalla Raghavendra Reddy, Raphaële J. Clément, Gopalakrishnan Sai Gautam, and Premkumar Senguttuvan*



Cite This: *Inorg. Chem.* 2024, 63, 14335–14344



Read Online

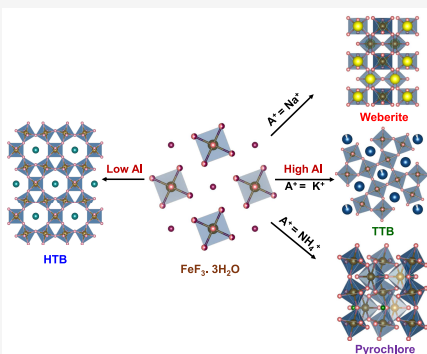
ACCESS |

Metrics & More

Article Recommendations

Supporting Information

ABSTRACT: Topochemical reactions are powerful pathways to modify inorganic extended structures, but the present approaches are limited by the degrees of freedom to tune the structural connectivity and dimensionality. In this work, we unveil a new topochemical bottom-up approach to tailor three-dimensional (3D) iron fluoride frameworks from the same one-dimensional (1D) $\text{FeF}_3 \cdot 3\text{H}_2\text{O}$ (IF) precursor upon reacting with iodide-based reagents (Al^- ; $\text{A}^+ = \text{Na}^+$, K^+ , and NH_4^+). To elucidate their formation mechanism, a series of topochemical reactions are performed by varying the concentration of precursors, reaction temperatures, and durations, and their corresponding products are analyzed through X-ray diffraction, nuclear magnetic resonance, and Mössbauer spectroscopy techniques. Although the lower molar ratio of Al:IF ($\approx 0.25:1.0$) produces the same hexagonal tungsten bronze (HTB)-type A_xFeF_3 , the topochemical reactions with higher Al:IF ratios yield weberite- $\text{Na}_{1.95}\text{Fe}_2\text{F}_7$, tetragonal tungsten bronze (TTB)- $\text{K}_{0.58}\text{FeF}_3$, and pyrochlore- $\text{NH}_4\text{Fe}_2\text{F}_6$ phases. Our density functional theory calculations attribute the formation of iron fluoride phases to their thermodynamic stability. Moreover, kinetics also play an important role in enabling weberite and HTB fluorides with high purity, while the pyrochlore- $\text{NH}_4\text{Fe}_2\text{F}_6$ retains a minor HTB-(NH_4) $_x\text{FeF}_3$ impurity. Overall, this work shows a new possibility of modulating the low-dimensional precursor to attain 3D frameworks with different structural arrangements *via* topochemical approaches.



INTRODUCTION

Chemical synthesis plays a central role in tailoring various classes of inorganic, organic, and hybrid materials. Solid-state reactions, which are widely practiced from the laboratory to industrial scale to produce inorganic materials, require high energy for the facile diffusion of reagents, thereby producing thermodynamically stable products. Although the recent progress in *in situ* X-ray diffraction^{1–4} and computational techniques^{5,6} have provided additional information regarding the formation mechanism of desired phases including metastable ones, the prediction of synthesis outcomes is still difficult as one cannot dictate the atomic diffusion processes occurring through conventional solid-state reactions. This situation is in stark contrast to organic synthesis, wherein molecular chemists employ retrosynthetic approaches to direct the atomic connectivity *via* solution-state sequential reactions for making targeted natural products, macromolecules, and supramolecular structures. Furthermore, organic crystals can be tailored using stereo- and regio-specific reactions between molecules confined in the lattice *via* crystal engineering approaches.⁷

While such direct control over atomic connectivity in extended inorganic structures is extremely challenging, soft chemical approaches, such as topochemical modulations, can modify cationic and/or anionic sublattices of a parent

framework.^{8,9} So far, various classes of oxides,¹⁰ fluorides,¹¹ sulfides,¹² phosphates,¹³ and mixed anionic frameworks^{14–16} have been synthesized using diverse topochemical approaches such as (de)intercalation, ion-exchange, and dehydration, which otherwise cannot be readily obtained through conventional solid-state reactions. Yet, the present topochemical approaches are restricted on two fronts: (i) the requirement of a thermodynamically stable phase first synthesized *via* solid-state synthesis and (ii) the limited degrees of freedom for tuning the structural connectivity and dimensionality since the processes occur in sequential steps.

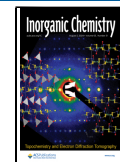
Recently, our group has demonstrated a novel topochemical bottom-up approach in which a one-dimensional (1D) $\text{FeF}_3 \cdot 3\text{H}_2\text{O}$ (IF) precursor is converted into 2D- NaFeF_4 and orthorhombic weberite 3D- $\text{Na}_2\text{Fe}_2\text{F}_7$ frameworks through the incorporation of a “structure-stabilizing agent”, NaF , into the host lattice.¹¹ Briefly, the formation of 2D- NaFeF_4 from $\text{FeF}_3 \cdot 3\text{H}_2\text{O}$ involves concurrent dehydration, ion exchange

Received: January 31, 2024

Revised: June 5, 2024

Accepted: June 19, 2024

Published: July 22, 2024



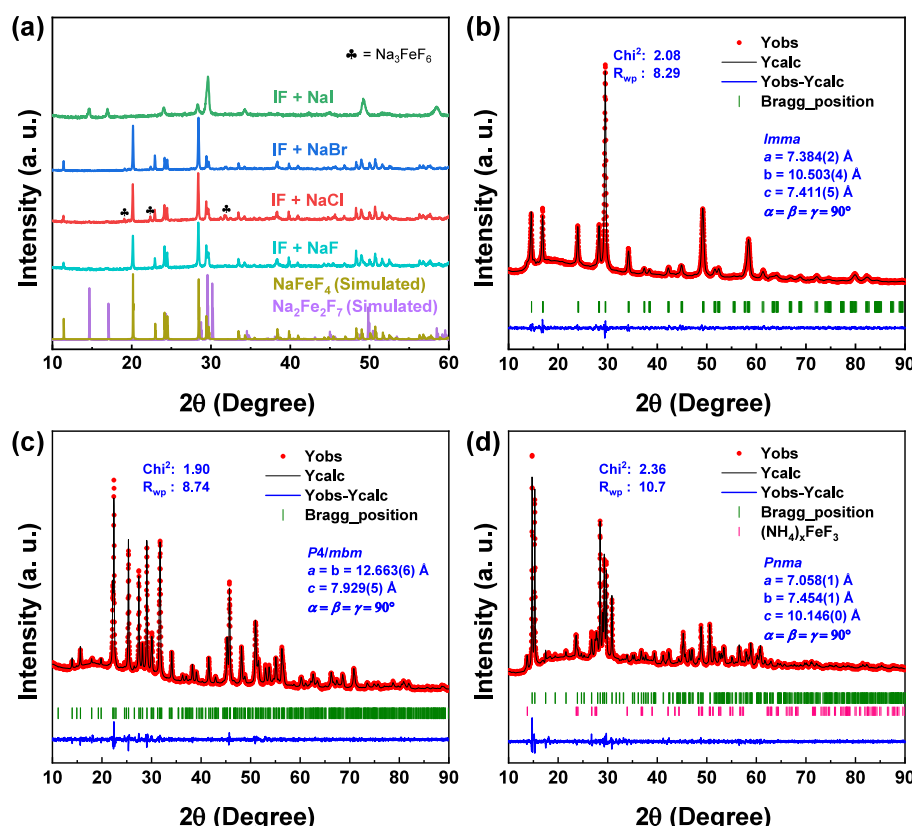


Figure 1. (a) Comparison of the XRD patterns collected on the products of reactions between IF and NaF/NaCl/NaBr/NaI. Rietveld analyses of the iron fluoride phases obtained by reacting (b) NaI, (c) KI, and (d) NH₄I with IF in a 1:1 molar ratio.

between Na⁺/F⁻ and H⁺/OH⁻ groups, and condensation of F⁻/OH⁻ groups. When the same reaction is carried out at a higher temperature (230 °C), the 3D-Na₂Fe₂F₇ framework forms through a minor rearrangement of the 2D framework upon topotactic fluoride deintercalation and iron reduction. It is worth noting that two other weberite polymorphs, monoclinic¹⁷ and trigonal Na₂Fe₂F₇,¹⁸ were prepared through a high-temperature synthesis route, while the topochemical bottom-up approach enabled the manipulation of IF precursor lattice to produce orthorhombic-Na₂Fe₂F₇. A recent study highlighted the presence of orthorhombic, monoclinic, and trigonal Na₂Fe₂F₇ polymorphs in the same sample prepared by high-energy ballmilling.¹⁹

Further, we have attempted to produce mixed-halide 2D-NaFeF₃Cl, -NaFeF₃Br, and -NaFeF₃I frameworks from an IF precursor by utilizing “NaCl/NaBr/NaI” as the corresponding structural stabilizing agents (for details, see **Experimental Section**). While the X-ray diffraction (XRD) patterns (**Figure 1a**) collected on the products of the reactions between IF and NaCl or NaBr resemble that of NaFeF₄, their corresponding energy-dispersive elemental mappings confirm the complete absence of chloride and bromide species (**Figure S1**). Furthermore, the Fourier-transformed infrared (FTIR) spectra reveal the presence of OH⁻ anions (**Figure S2a**) in the samples. These observations suggest that the products of the reactions between IF and NaCl/NaBr belong to the NaFeF_{4-x}(OH)_x family of compounds. Interestingly, the reaction between NaI and IF at 130 °C has been found to lead to 3D-Na₂Fe₂F₇ due to the redox activity of the I⁻/I₂ redox couple,^{20–23} which opens new avenues to tailor 3D iron fluoride frameworks using iodide-based reagents. Previously,

LiI and NaI reagents were used to synthesize Li- and Na-intercalated transition metal oxides through a topotactic intercalation reaction.

Along those lines, herein, we report the direct formation of three different 3D iron fluoride frameworks from the same 1D-FeF₃·3H₂O precursor through the addition of iodide-based reagents (Al; A⁺ = Na⁺, K⁺, and NH₄⁺). We investigate their formation mechanisms and the underlying thermodynamic and kinetic factors using XRD, nuclear magnetic resonance (NMR) spectroscopy, and density functional theory (DFT) calculations.^{24,25} While the formation of 3D frameworks is dictated by the different knitting of 1D chains from the precursor, their phase purity is affected by the temperature and reaction time of topochemical synthesis.

RESULTS AND DISCUSSION

The reaction between Al and IF in a 1:1 mole ratio was performed in tetraethylene glycol (TEG) solvent at 130 or 170 °C for 6 h (see **Experimental Section** for details). Rietveld analysis of the powder XRD patterns collected on the products and the corresponding cell parameters are displayed in **Figure 1b–d** and summarized in **Tables S1–S3**, respectively. As discussed earlier, the reaction between NaI and IF produces orthorhombic weberite-Na₂Fe₂F₇ (space group: *Imma*), whereas the reactions utilizing KI and NH₄I yield tetragonal tungsten bronze (TTB)-K_xFeF₃ (0.4 < x < 0.6)^{26,27} and pyrochlore-NH₄Fe₂F₆ phases, respectively.^{28,29} Note that pyrochlore-NH₄Fe₂F₆ sample contains a minor hexagonal tungsten bronze (HTB)-(NH₄)_xFeF₃ (0.18 ≤ x ≤ 0.4) impurity phase as well. Inductively coupled plasma-optical emission spectroscopy (ICP-OES) analyses of weberite and TTB samples indicate

compositions of $\text{Na}_{1.99(5)}\text{Fe}_{1.99(9)}\text{F}_7$ and $\text{K}_{0.58(1)}\text{Fe}_{0.99(9)}\text{F}_3$, respectively. Mössbauer experiments were performed on the weberite, HTB, and pyrochlore samples to quantify the $\text{Fe}^{3+}/\text{Fe}^{2+}$ ratio (Figures S3a–c) and the corresponding fitting parameters are provided in Table S4. While the $\text{Fe}^{3+}/\text{Fe}^{2+}$ ratio (47:53) for the TTB sample almost matches that derived from the composition estimated with ICP, the higher Fe^{3+} content in the pyrochlore sample ($\text{Fe}^{3+}/\text{Fe}^{2+} \sim 68:32$) is probably due to the presence of the HTB impurity. Similarly, the weberite sample also shows a higher Fe^{3+} content ($\text{Fe}^{3+}/\text{Fe}^{2+} \sim 70:30$) than expected based on the ICP composition, due to the presence of an amorphous Na_3FeF_6 -type impurity as deduced from ^{23}Na nuclear magnetic resonance spectroscopy (NMR) measurement (Figure S3d). While the FTIR spectra of the products from NaI- and KI-based reactions show no signature of OH^- features (Figure S2b), the presence of NH_4^+ in the pyrochlore phase is confirmed by the features at 3250 and 1427 cm^{-1} (due to N–H stretching and N–H bending modes, respectively).³⁰ Furthermore, scanning electron microscopy (SEM) analysis of the weberite, HTB, and pyrochlore samples shows a significant reduction of their particle sizes compared to the IF precursor (Figure S5), which may be due to the dehydration reaction.³¹

To better understand the distribution of Na local environments in the weberite $\text{Na}_2\text{Fe}_2\text{F}_7$ sample, ^{23}Na solid-state nuclear magnetic resonance (ss-NMR) experiments were conducted. The presence of $\text{Fe}^{2+}/\text{Fe}^{3+}$ species in $\text{Na}_2\text{Fe}_2\text{F}_7$ (as well as in the other IF framework structures discussed later) leads to strong paramagnetic interactions between the unpaired electron spins on Fe and the ^{23}Na nuclear spins under consideration and significant ^{23}Na NMR line broadening and large chemical shifts. Additionally, as ^{23}Na is a quadrupolar nucleus ($I = 3/2$), the resulting ^{23}Na NMR spectra are further broadened and shifted due to quadrupolar effects. The ^{23}Na solid-state NMR spectrum for NaI-IF weberite is shown in Figure S3d. The asterisks denote sidebands arising from the fast rotation of the sample during NMR data acquisition, which are suppressed in the overlaid ^{23}Na pj-MATPASS³² NMR spectrum. The pj-MATPASS spectrum consists of overlapping ^{23}Na resonances with chemical shifts in the range of 100 and 800 ppm, which are ascribed to several ^{23}Na local environments in weberite $\text{Na}_2\text{Fe}_2\text{F}_7$ at 7.35 T.¹⁹ An additional signal is observed near 1750 ppm, which we assign to Na nuclei in an amorphous Na_3FeF_6 impurity phase based on a previous report³³ and given that this compound is not observed by XRD. The presence of a small amount of amorphous Na_3FeF_6 impurity is consistent with the metastability of weberite- $\text{Na}_2\text{Fe}_2\text{F}_7$ and the presence of an adjacent, thermodynamically stable cryolite-like Na_3FeF_6 phase in the Na–Fe–F phase diagram.¹⁹

A fit of the quantitative ^{23}Na spin echo spectrum (Figure S4) provides additional insight into the total number of paramagnetic Na environments in the sample. The ^{23}Na spectrum can be fit using four components. Two of these four resonances arise from the two crystallographic Na sites in the amorphous Na_3FeF_6 impurity, and their chemical shifts ($\delta = 350$ and 1750 ppm) and intensity ratio (2:1) were fixed in the fitting procedure to match the previously reported spectral line shape for this compound.³³ Their combined integrated intensities indicate that the Na_3FeF_6 impurity accounts for $5 \pm 2\%$ of the total Na molar content in the sample. The chemical shifts of the other two ^{23}Na resonances are consistent with the Na species in $\text{Na}_2\text{Fe}_2\text{F}_7$ weberite structural variants. Yet only the

orthorhombic variant is observed by XRD, with two crystallographic Na sites, which suggests the presence of a second, minor, and poorly crystalline phase that cannot easily be observed by laboratory XRD. Overall, the ^{23}Na NMR results are consistent with the presence of a major orthorhombic $\text{Na}_2\text{Fe}_2\text{F}_7$ weberite phase, a minor amorphous Na_3FeF_6 impurity, and a minor and poorly crystalline $\text{Na}_2\text{Fe}_2\text{F}_7$ phase.

These results indicate that reactions initiated with the same IF:Al molar ratio (i.e., 1:1), produce three different iron fluoride compounds with different structural frameworks and different A/Fe atomic ratios. While the modulations of the parent IF structure to the product structures can be rationalized by comparing their structural topologies (which will be detailed later), the remaining question is what thermodynamic and kinetic factors drive these topochemical reactions to yield different products. To better understand this, we performed a series of topochemical reactions with varying Al:IF molar ratio, time, and temperature and studied their corresponding products *via* XRD. First, we heated the IF precursor by itself (i.e., without Al) to 130 °C in TEG for various time lengths, from 1.5 to 6 h (Figure S6). At 1.75 h of reaction time, the XRD reflections corresponding to the IF precursor become weaker, with little to no sign of a secondary phase. After 2 h at 130 °C, however, the HTB- $\text{FeF}_3\cdot0.33\text{H}_2\text{O}$ phase starts to appear.^{34,35}

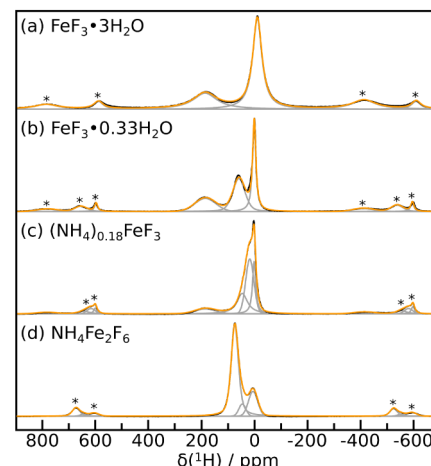


Figure 2. ^1H ss-NMR spin echo spectra collected on (a) $\text{FeF}_3\cdot3\text{H}_2\text{O}$, (b) $\text{FeF}_3\cdot0.33\text{H}_2\text{O}$, (c) $(\text{NH}_4)_{0.18}\text{FeF}_3$, and (d) $\text{NH}_4\text{Fe}_2\text{F}_6$ along with fits of individual resonances. For each compound, the spectrum is shown in black, the overall fit in orange, and individual resonances in gray. Spinning sidebands are indicated by an asterisk.

The formation of HTB- $\text{FeF}_3\cdot0.33\text{H}_2\text{O}$ from the IF precursor was further investigated through ^1H ss-NMR (Figure 2). The ^1H NMR spectrum of the IF precursor (Figure 2a) exhibits two paramagnetically broadened signals centered at $\delta = -9$ and 188 ppm, with line widths of 42 and 109 ppm, respectively (summary of ^1H ss-NMR fits in Table S5), suggesting that the corresponding ^1H species are spatially close to Fe species. The sharper resonance at -9 ppm is attributed to isolated H_2O molecules in the IF framework (i.e., not directly connected to FeF_6 octahedra),³⁴ and the broader resonance at 188 ppm is assigned to H_2O units occupying equatorial positions within the $\text{FeF}_{6-x}(\text{H}_2\text{O})_x$ (x between 0 and 4) chains, the latter being both closer and directly bonded to paramagnetic Fe species.

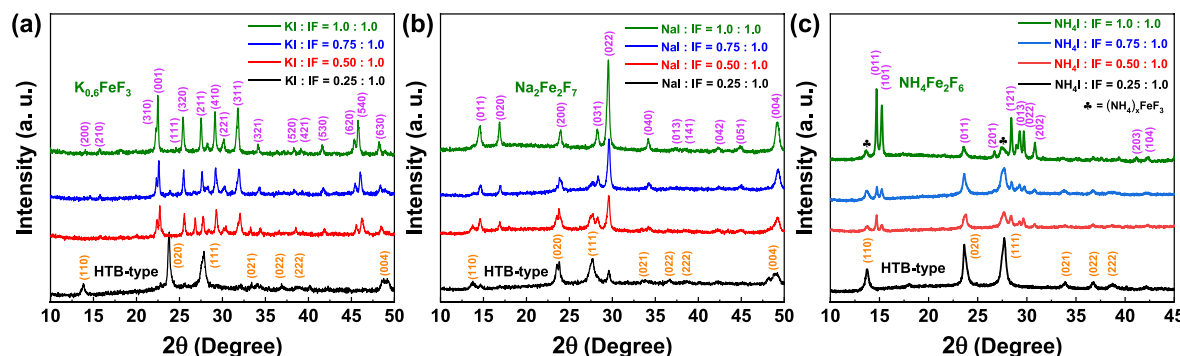


Figure 3. XRD patterns of iron fluoride phases obtained from the reactions between Al and IF with varied amounts of (a) NaI, (b) KI, and (c) NH₄I.

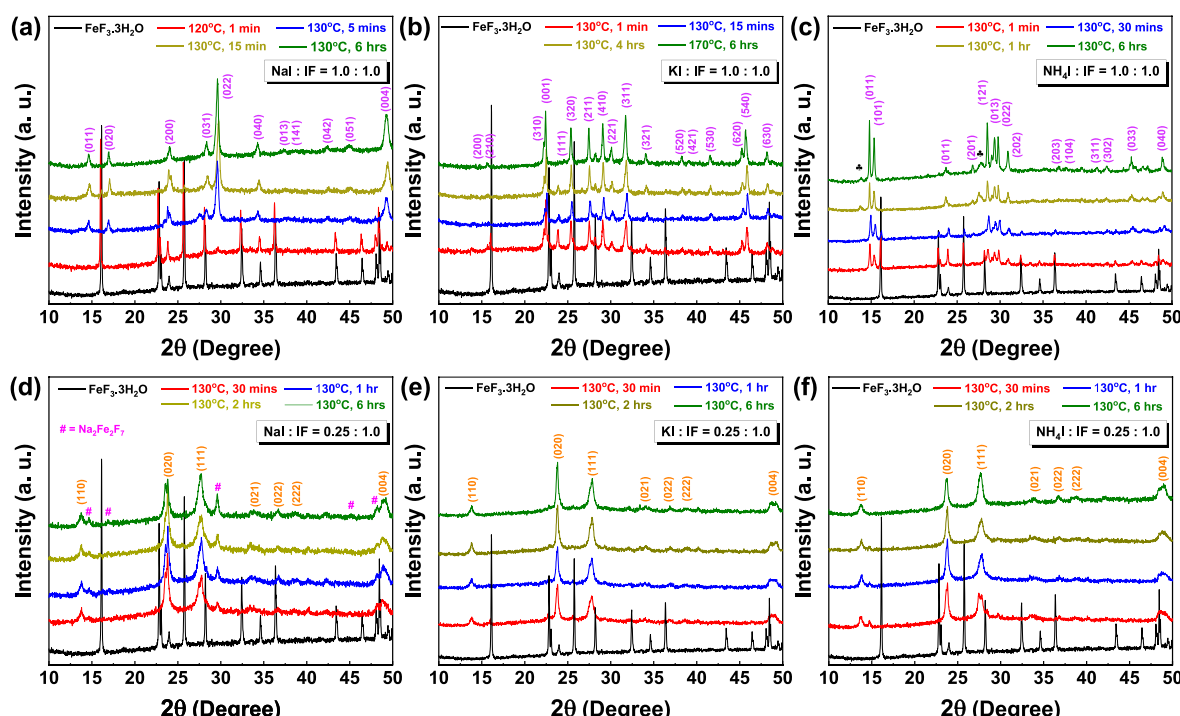


Figure 4. XRD patterns during the evolution of phases while heating IF with NaI, KI, and NH₄I in (a–c) 1.0:1.0 and (d–f) 0.25:1.0 ratios at different temperatures and time durations.

The sharp signal at $\delta = 2$ ppm in the ^1H NMR spectra of HTB- $\text{FeF}_3\cdot 0.33\text{H}_2\text{O}$ (Figure 2b) likely corresponds to isolated H_2O molecules now located in the large cavities of the HTB structure, leading to reduced paramagnetic broadening (and a slightly reduced shift) as compared to isolated H_2O molecules in the IF framework, while the broad signal at $\delta = 187$ ppm is similar to that observed for the IF and is therefore assigned to H_2O molecules within the $\text{FeF}_{6-x}(\text{H}_2\text{O})_x$ chains. The third broad signal centered at $\delta = 60$ ppm is hypothesized to also arise from coordinated H_2O , or perhaps OH^- units within the $\text{FeF}_{6-x}(\text{H}_2\text{O})_x$ chains, but in a slightly different local environment as compared to the H_2O molecules resonating at 187–188 ppm. Those results overall indicate that the transformation of IF to HTB- $\text{FeF}_3\cdot 0.33\text{H}_2\text{O}$ is driven *via* dehydration and condensation reactions.³¹

Next, we studied the influence of the Al:IF molar ratio on the formation of different 3D phases since the A/Fe atomic ratio decreases from weberite- $\text{Na}_2\text{Fe}_3\text{F}_7$, to TTB- $\text{K}_2\text{Fe}_3\text{F}_3$ ($0.4 <$

$x < 0.6$), to pyrochlore- $\text{NH}_4\text{Fe}_2\text{F}_6$. We carried out reactions between AI and IF precursors in different molar ratios at 130 °C for 6 h, and the corresponding XRD patterns collected on the reaction products are shown in Figure 3a–c. In the case of reactions between NaI and IF in a molar ratio of 0.25:1, HTB-type Na_xFeF_3 ($0.1 < x < 0.3$)³⁶ and weberite- $\text{Na}_2\text{Fe}_2\text{F}_7$ are formed. As the concentration of NaI is increased in the precursor mixture, the XRD peaks correspond to HTB-type Na_xFeF_3 are reduced in intensity, while those corresponding to the weberite- $\text{Na}_2\text{Fe}_2\text{F}_7$ phase grow. Similar observations are noted for the KI and NH_4I -based reactions. At the lower KI:IF and NH_4I :IF ratio (0.25:1), HTB-type K_xFeF_3 and $(\text{NH}_4)_x\text{FeF}_3$ phases are produced, whereas the reactions with higher concentrations of iodide reagents yield TTB and pyrochlore phases, respectively, but with minor HTB-type impurities. The formation of HTB- $(\text{NH}_4)_x\text{FeF}_3$ and pyrochlore- $\text{NH}_4\text{Fe}_2\text{F}_6$ is also monitored via ^1H NMR measurements (Figure 2). In the ^1H ss-NMR spectrum for HTB-

$(\text{NH}_4)_x\text{FeF}_3$ (Figure 2c), a sharp signal at $\delta = 2$ ppm and a broader signal at $\delta = 187$ ppm (Table S5) are observed similar to those for HTB- $\text{FeF}_3\cdot 0.33 \text{ H}_2\text{O}$, suggesting the presence of similar ^1H environments in the cavities and within the $\text{FeF}_{6-x}(\text{H}_2\text{O})_x$ chains of the structure. The remaining signals at $\delta = 19$ and 47 ppm are tentatively assigned to NH_4^+ units in the HTB framework. In the case of pyrochlore- $\text{NH}_4\text{Fe}_2\text{F}_6$ (Figure 2d), a dominant broad signal is observed at $\delta = 76$ ppm, which is likely associated with NH_4^+ in the pyrochlore framework. The other two signals at $\delta = 7$ and 47 ppm (Table S5) are likely due to the remnant HTB-($\text{NH}_4)_x\text{FeF}_3$ impurity phase in the sample on the basis of their chemical shifts. At this point, an intriguing question arises: why can phase pure TTB and pyrochlore not be obtained despite utilizing excess Al?

Furthermore, we performed topochemical reactions at a fixed molar ratio of Al and IF at 130 °C for different time durations. In the case of reactions with Al:IF ≈ 1:1, the appearance of weberite- $\text{Na}_2\text{Fe}_2\text{F}_7$, TTB- K_xFeF_3 , and pyrochlore- $\text{NH}_4\text{Fe}_2\text{F}_6$ phases are noticed along with minor HTB-type phases within 1–5 min (see Figure 4a–c). While the phase purity of weberite- $\text{Na}_2\text{Fe}_2\text{F}_7$ is greatly improved upon extending the reaction time to 6 h, KI- and NH_4I -based reaction products still contained minor HTB- K_xFeF_3 and HTB-($\text{NH}_4)_x\text{FeF}_3$, respectively. Notably, the phase purity of TTB- K_xFeF_3 is increased upon increasing the reaction temperature to 170 °C (Figure S7); however, the same attempt with the NH_4I and IF reactions was futile in improving the phase purity (Figure S8).

Additionally, we performed the reactions with Al:IF ≈ 0.25:1 (Figure 4d–f) under experimental conditions similar to those previously described. In the case of the NaI/IF reactions, the product collected after 30 min shows the formation of HTB- Na_xFeF_3 with weberite- $\text{Na}_2\text{Fe}_2\text{F}_7$ as a secondary phase. As the reaction time is increased to 6 h, the peak intensities of weberite- $\text{Na}_2\text{Fe}_2\text{F}_7$ increase at the expense of HTB- Na_xFeF_3 . On the contrary, the XRD patterns recorded on the products from KI/IF and NH_4F /IF reactions (from 30 min to 6 h) show only the presence of HTB- K_xFeF_3 and ($\text{NH}_4)_x\text{FeF}_3$ phases. The estimated $\text{Fe}^{3+}/\text{Fe}^{2+}$ ratios from Mössbauer experiments suggest the composition of HTB phases as HTB- $\text{Na}_{0.03}\text{FeF}_3$, - $\text{K}_{0.05}\text{FeF}_3$, and -($\text{NH}_4\right)_{0.16}\text{FeF}_3$ (Figure S9 and Table S4). To better understand the discrepancies among the formations of pure HTB- A_xFeF_3 phases, we performed another set of reactions in which HTB- A_xFeF_3 phases harvested after 1 h were used as the precursors along with 0.75 mol of Al (Figure S10). While the reaction of HTB- Na_xFeF_3 with additional NaI shows enhanced peak intensities of the weberite phase, no noticeable changes are observed for the KI- and NH_4I -based reactions. The conversion of HTB- Na_xFeF_3 to weberite- $\text{Na}_2\text{Fe}_2\text{F}_7$ can be ascribed to the greater thermodynamic metastability of the former, as discussed later in the manuscript.

To better understand the thermodynamic stability of iron fluoride compounds, DFT calculations were performed on the A–Fe–F phases of interest to this work. Figure 5 shows the energy above and below the convex hull (E^{Hull}) of various iron fluorides (i.e., HTB, TTB, perovskite, AFeF₄, pyrochlore, and weberite) within their respective ternary phase diagram, where blue, orange, and purple bars represent sodium-, potassium-, and ammonium-based iron fluorides, respectively. The horizontal dashed green line represents the rule-of-thumb of $E^{\text{Hull}} = 50$ meV/atom as a threshold for experimental synthesizability.^{37,38} The convex hull of each iron fluoride

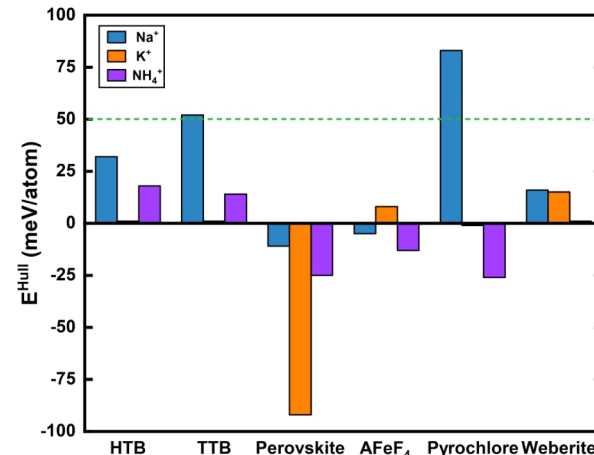


Figure 5. Energy above and below the convex hull (E^{Hull}) of Na^+ , K^+ , or NH_4^+ in a representative iron fluoride framework such as HTB, TTB, perovskite, AFeF₄, pyrochlore, and weberite, calculated from our ternary phase diagram. The blue, orange, and purple bars indicate sodium-, potassium-, and ammonium-based iron fluorides, respectively. The horizontal dashed green line represents the rule-of-thumb of $E^{\text{Hull}} = 50$ meV/atom as a threshold for experimental synthesizability.³⁸

framework is depicted in Figure S17, while adjacent phases of stable iron fluoride frameworks and decomposition products of unstable or metastable iron fluoride frameworks are listed in Tables S6 and S7, respectively.

Based on our calculated convex hull, perovskite- NaFeF_3 (−11 meV/atom) and NaFeF_4 (−5 meV/atom) frameworks lie on the convex hull, where the negative E^{Hull} values indicate the formation energies from nearby stable phases in the chemical space, highlighting the stability of these frameworks, in good agreement with the perovskite phase being known as stable,³⁹ while the 2D NaFeF_4 framework is experimentally realized.^{11,40} In contrast, the E^{Hull} of weberite- $\text{Na}_2\text{Fe}_2\text{F}_7$ (16 meV/atom) and HTB- $\text{Na}_{0.25}\text{FeF}_3$ (32 meV/atom) phases are positive, indicating that they lie above the convex hull, while their magnitudes are within the range of tolerance limit of $E^{\text{Hull}} = 50$ meV/atom, which is expected to be stabilized at higher temperatures. Indeed, this agrees with our experimental finding that we successfully synthesized the weberite- $\text{Na}_2\text{Fe}_2\text{F}_7$ phase at 130 °C from IF by using NaI as a reducing agent. Note that our convex hull calculation suggests FeF_2 , NaFeF_4 , and Na_3FeF_6 as decomposition products, which aligns well with the observation of a small amount of Na_3FeF_6 impurity in the product of the reaction between NaI and IF (see Figure S2d). Notably, at higher temperatures, a phase exhibiting greater compositional, vibrational, and/or configurational degrees of freedom experiences a favorable increase in entropy compared to highly ordered phases. For instance, at higher temperatures, the metastable weberite- $\text{Na}_2\text{Fe}_2\text{F}_7$ (16 meV/atom at 0 K) could potentially be stabilized over predicted stable, ordered competing phases like NaFeF_4 (−5 meV/atom at 0 K) due to its higher compositional and configurational degrees of freedom.

Similarly, the HTB- $\text{Na}_{0.25}\text{FeF}_3$ phase is observed during the reaction of the IF precursor when using a low NaI mole fraction. Given its metastable nature, the addition of extra NaI in the reaction leads to its transformation to the weberite phase. On the contrary, the TTB- $\text{Na}_{0.6}\text{FeF}_3$ (52 meV/atom) and pyrochlore- NaFe_2F_6 (83 meV/atom) phases exhibit

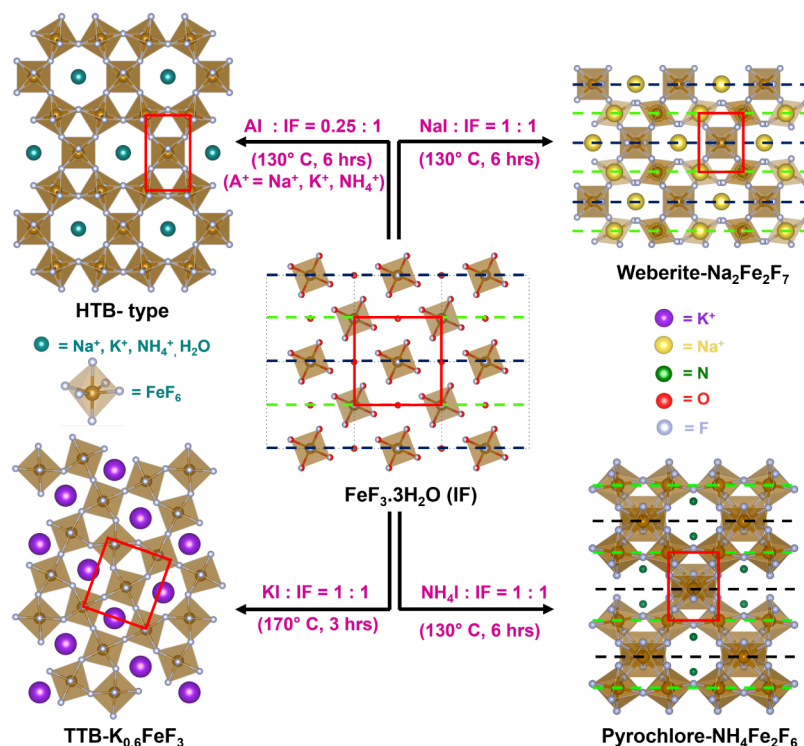


Figure 6. Mechanistic pathway and specific reaction conditions for the formation of various iron fluoride compounds from the IF precursor with different AlIs.

significantly higher E^{Hull} values, exceeding the synthesizability threshold of $E^{\text{Hull}} = 50$ meV/atom, suggesting the instability of these phases; evidently, we did not observe these phases during the synthesis of Na-based iron fluoride frameworks. Based on our 0 K convex hull, we infer that the TTB and pyrochlore Na–Fe–F phases are not likely to be stable and synthesized and will decompose to more stable phases. In the case of K-based iron fluorides, the perovskite-KFeF₃ phase unsurprisingly exhibits a large negative E^{Hull} value of -92 meV/atom, which lies on the convex hull, indicating the higher stability of this phase. In addition, the E^{Hull} of pyrochlore-KFe₂F₆ lies below the convex hull with a minimal E^{Hull} value of -1 meV/atom, suggesting the stability of this phase as well. On the contrary, the E^{Hull} value for HTB-K_{0.25}FeF₃ (~ 1 meV/atom), TTB-K_{0.6}FeF₃ (~ 1 meV/atom), KFeF₄ (~ 8 meV/atom), and weberite-K₂Fe₂F₇ E^{Hull} (15 meV/atom) phases are marginally positive, with these phases lying above the convex hull but within the tolerance of experimental synthesizability limit. Evidently, we have successfully synthesized the TTB-K_{0.6}FeF₃ framework from the reaction between KI and IF, while the HTB-K_{0.25}FeF₃ phase was also noticed during this reaction, both of which are only marginally above the convex hull (~ 1 meV/atom) and can be stabilized at room or higher temperatures. Although we predict the KFeF₄ and K₂Fe₂F₇ phases to be metastable, they are not observed during the reaction between KI and IF, likely due to kinetic reasons.

Similarly, in the case of NH₄-based iron fluorides, the pyrochlore-NH₄Fe₂F₆ phase is stable with an E^{Hull} of -26 meV/atom, in line with our experimental observation. In addition, perovskite-NH₄FeF₃ and NH₄FeF₄ frameworks are also stable despite not being observed in our experiments. The other NH₄-containing phases are metastable with an E^{Hull} of 18 meV/atom for HTB-(NH₄)_{0.25}FeF₃, 14 meV/atom for TTB-(NH₄)_{0.6}FeF₃, and 1 meV/atom for weberite-(NH₄)₂Fe₂F₇,

suggesting that these phases may be encountered during high temperature synthesis reactions. Note that the (meta)stability of the HTB-(NH₄)_{0.25}FeF₃ phase is in good agreement with our experimental observation, where this phase is noticed during the reaction between NH₄I at low mole fraction and IF, with the thermodynamic driving force to form the stable pyrochlore phase resulting in the reduction of the phase fraction of the HTB phase at higher temperatures and longer reaction times. However, the fact that the HTB impurity is never fully removed from our reactions may be attributed to kinetic reasons. Overall, our DFT-based thermodynamic stability investigation suggests that the observed structural variation of topochemically synthesized iron fluorides upon insertion of different cations can be largely attributed to the thermodynamic (in)stability of the respective frameworks.

CONCLUSIONS

In conclusion, the present study highlights the dependence of the formation of specific iron fluoride phases on the Al:IF precursor molar ratio, reaction temperature, and time. We show that lower Al:IF molar ratios (0.25:1) produce similar HTB-A_xFeF₃ iron fluoride frameworks, and increased Al (NaI, KI, and NH₄I) concentrations lead to the formation of weberite, TTB, and pyrochlore phases, respectively, due to their thermodynamic stability. While high phase purity is achieved for the Na-weberite compound at a relatively low temperature (130 °C), high-temperature annealing is necessary to produce phase-pure TTB-K_xFeF₃, indicating that kinetics play an important role in its formation. We note that all our synthesis attempts failed to form a pure pyrochlore phase despite its thermodynamic stability. Importantly, the formation of weberite, TTB, and pyrochlore phases occurs directly from the IF framework without the formation of intermediate HTB phases. Based on these observations, we tentatively propose

the following formation mechanism of iron fluoride phases from the IF precursor **Figure 6**:

(a) The formation of HTB phases occurs *via* concurrent dehydration, ion exchange, and condensation reactions.³¹ As the topochemical reaction proceeds, each 1D chain ($[FeF_6]_n$ and $[Fe_2(H_2O)_4]_n$)³⁴ in the IF framework knits with four other 1D chains to form hexagonal tunnels that are filled with A^+ cations. Similarly, the formation of the TTB- K_xFeF_3 phase can be described as the condensation of 1D chains; however, the linkages of 1D chains in HTB and TTB phases are different, resulting in three different types of channels in TTB.

(b) Unlike in previous cases, the conversion of IF to weberite and pyrochlore phases requires more significant structural rearrangements. For the weberite phase, half of the 1D chains (indicated by blue dotted lines in **Figure 4**) in the IF framework break into individual FeF_6 units to pillar the remaining 1D chains (indicated by green dotted lines), resulting in the 3D weberite phase with Na^+ -ions occupying the atomic positions of H^+ -ions in H_2O . Similar transformations are required for the formation of pyrochlore but with the reknitting of broken individual FeF_6 units to produce chains that run parallel to [1 0 0] and [0 1 0] directions of the pyrochlore structure (**Figure S18**).

EXPERIMENTAL SECTION

Materials. Sodium fluoride (NaF, Alfa Aesar, 99.5%), sodium chloride (NaCl, Alfa Aesar, 99.5%), sodium bromide (NaBr, Alfa Aesar, 99.5%), sodium iodide (NaI, Alfa Aesar, 99.5%), potassium iodide (KI, Sigma-Aldrich, 99%), ammonium iodide (NH_4I , Sigma-Aldrich, 99%), iron(III) fluoride trihydrate ($FeF_3 \cdot 3H_2O$, Sigma-Aldrich), and tetraethylene glycol (TEG, Alfa Aesar, 99%) were used for synthesis without further purification.

Synthesis. All the products were synthesized by the solvothermal method. First, a 1:1 stoichiometric ratio of AI ($A^+ = Na^+, K^+, and NH_4^+$) and $FeF_3 \cdot 3H_2O$ (IF) was taken in a Teflon-lined autoclave along with 10 mL of TEG. The autoclave was then placed in an oil bath and the mixture was continuously stirred at room temperature for several hours. Then, the temperature was gradually increased (1 °C/min) to certain temperatures, dwelled for different time durations, and then cooled to room temperature. Reacting NaI with IF at 130 °C for 6 h produces a pure weberite- $Na_2Fe_2F_7$ phase, while for TTB and pyrochlore phase synthesis, the reaction temperature must be raised to 170 °C. The same procedure is followed for the attempted synthesis of 2D- $NaFeF_3(Cl/Br)$ frameworks where NaCl, and NaBr were used along with IF and reacted at 150 °C for 6 h. Next, the obtained products were centrifuged, washed with ethanol and acetone multiple times, and finally dried in a vacuum oven at 60 °C for 5 h. The yield of each reaction was ~75% with respect to the amount of iron fluoride precursor used. The iron fluoride precursor and the formed products at different conditions were stored in a desiccator or sometimes in a glovebox to avoid any degradation or HF formation.

Material Characterization. Powder X-ray diffraction of the samples was performed using Cu source having $K\alpha_1$ and $K\alpha_2$ ($\lambda = 1.54056$ and 1.54439 Å, respectively) radiation in a Rigaku X-ray diffractometer. The structural refinements and Rietveld analysis were performed with the help of FULLPROF suits. FESEM was performed using a Zeiss, Gemini SEM 500, FEI Inspect F 50 operating at 10 kV. PIKE technologies GladiATR instrument was used to record the FTIR data.

¹H and ²³Na solid-state NMR spectra were collected on a Bruker Avance 100 MHz (2.35 T, ¹H Larmor frequency of 100 MHz) wide-bore NMR spectrometer and a 300 MHz (7.05 T, ²³Na Larmor frequency of 79.39 MHz) ultrawide-bore NMR spectrometer, respectively, at room temperature. Data were obtained at 60 kHz magic-angle spinning (MAS) by using a 1.3-mm double-resonance HX probe. ¹H and ²³Na NMR data were referenced against adamantane [$(CH)_4(CH_2)_6, \delta(^1H) = 1.8$ ppm] and sodium chloride solutions (NaCl, $\delta(^{23}Na) = 0$ ppm), respectively, and these samples were also used for pulse calibration. Data were processed using the Bruker TopSpin 4.0.8 software, and spectra were fitted using the DMfit software.⁴¹ ¹H spin echo spectra were acquired using a 90° radiofrequency (RF) pulse of 1 μ s and a 180° RF pulse of 2 μ s at 15.6 W with a recycle delay of 30 ms. ²³Na spin-echo spectra were acquired by using a 90° radiofrequency (RF) pulse of 0.375 μ s and a 180° RF pulse of 0.75 μ s at 200 W. A recycle delay between 1 and 50 ms was used, with exact values optimized to ensure that the entire ²³Na signal was fully relaxed between pulses. ²³Na pj-MATPASS (projected Magic-Angle Turning Phase-Adjusted Sideband Separation)³² isotropic spectra were also acquired using a 90° RF pulse of 0.375 μ s at 200 W, with a recycle delay of 0.005 s.

⁵⁷Fe Mössbauer measurements were performed in transmission mode with a ⁵⁷Co radioactive source in constant acceleration mode using a standard PC-based Mössbauer spectrometer equipped with a WissEl velocity drive. Velocity calibration of the spectrometer was performed with natural iron absorber at room temperature. The spectra were analyzed with NORMOS program. The obtained hyperfine parameters from the high-field Mössbauer data are summarized in **Table S4**.

COMPUTATIONAL METHODS

DFT Calculations. Spin-polarized ground-state total energies were calculated using DFT as implemented in the Vienna ab initio simulation package (VASP),^{42,43} with the usage of the frozen core projector-augmented wave (PAW) potentials.⁴⁴ The elemental, binary, and experimentally observed ternary iron fluoride structures, including the perovskite phase, were obtained from the inorganic crystal structure database (ICSD),⁴⁵ with the exception of the weberite structure, which was obtained from ref. 46. A schematic of the structures used in our calculations is given in **Figures S11–S14**.

The structures of phases that were not observed during experimental synthesis are generated by inserting the cations of interest into experimentally observed and well-known iron fluoride (i.e., $K_{0.25}FeF_3$, $K_{0.6}FeF_3$, $NaFeF_4$, $NH_4Fe_2F_6$, and $Na_2Fe_2F_7$) structures obtained from ICSD, as illustrated in **Figures S11–S14**. For instance, ammonium-based and potassium-based weberite structures were obtained by substituting NH_4 and K at the Na site of sodium-based weberite ($Na_2Fe_2F_7$). The same approach is followed to generate other compositions as well. The perovskite $KFeF_3$ and $NaFeF_3$ were used to generate the cubic and orthorhombic perovskite polymorphs, respectively.

We used the Hubbard U -corrected strongly constrained and appropriately normed (i.e., SCAN+ U) exchange-correlation functional since prior studies have shown that it better predicts the experimental formation enthalpy of 3d transition metal oxides [3,4].^{47–49} An optimal U value of 3.6 eV is used for Fe in iron fluorides, which is obtained by fitting the DFT-

calculated oxidation energies of binary iron fluorides (i.e., $\text{FeF}_2/\text{FeF}_3$) with that of experimental formation enthalpy (see Figure S16). We used a plane wave kinetic energy cutoff of 520 eV and Gaussian smearing with a width of 0.05 eV to integrate the Fermi surface. For sampling the reciprocal lattice, a Γ -point-centered k -point mesh Monkhorst-Pack of at least $32/\text{\AA}$ density is chosen.⁵⁰ The ground-state structural relaxation was performed by fully relaxing the atomic positions, cell shape, and cell volume, without any symmetry constraints, until the total energy and atomic forces were converged to 10^{-5} and $10.031 \text{ eV}/\text{\AA}$, respectively. We considered both ferromagnetic (FM) and antiferromagnetic (AFM) orderings of iron fluorides to identify the correct ground-state structure (Figure S15).

To investigate the thermodynamic stability of experimentally observed iron fluoride frameworks (i.e., HTB, TTB, AFeF_4 , pyrochlore, and weberite), we constructed a 0 K convex hull (A–Fe–F) using the pymatgen package⁵¹ as demonstrated in Figure S17. For 0 K convex hull construction, we considered all possible elemental (Na, K, N, H, F, and Fe), binary (NaF , KF , NH_4 , FeF_2 , and FeF_3), and ternary (Na_3FeF_6 , $\text{Na}_5\text{Fe}_3\text{F}_{14}$, K_2FeF_5 , $\text{K}_4\text{Fe}_3\text{F}_{12}$, $\text{K}_3\text{Fe}_3\text{F}_{19}$, and $(\text{NH}_4)_2\text{FeF}_5$) configurations, whose ordered structures are available in the inorganic crystal structure database (ICSD). Note that the (in)stability of iron fluoride frameworks are also considered with respect to each experimentally observed polymorph and the perovskite phase (e.g., stability of $\text{Na}_2\text{Fe}_2\text{F}_7$ with respect to TTB- $\text{Na}_{0.6}\text{FeF}_3$, HTB- $\text{Na}_{0.25}\text{FeF}_3$, NaFeF_4 , pyrochlore- NaFeF_6 , and perovskite- NaFeF_3). After constructing the convex hull, we calculated energy above/below the convex hull (E^{Hull})⁵² to quantify the extent of stability or instability of phases (Figure 3).

■ ASSOCIATED CONTENT

Data Availability Statement

All the computational data presented in this study are freely available to all on our GitHub repository (<https://github.com/sai-mat-group/fe-fluorides-project>).

■ Supporting Information

The Supporting Information is available free of charge at <https://pubs.acs.org/doi/10.1021/acs.inorgchem.4c00425>.

FTIR, Mössbauer, ^{23}Na ss-NMR and ^1H ss-NMR, FESEM, additional XRD data, crystal structures of different iron fluoride frameworks and the magnetic configurations of Fe atoms, reaction enthalpy variation with increasing U, convex hull using DFT. Table for structural details, E^{Hull} calculations, Mössbauer analysis, and ^1H ss-NMR fitting parameters ([PDF](#))

■ AUTHOR INFORMATION

Corresponding Author

Premkumar Senguttuvan – New Chemistry Unit, Bangalore, Jakkur 560064, India; International Centre for Materials Science, Bangalore, Jakkur 560064, India; School of Advanced Materials, Jawaharlal Nehru Centre for Advanced Scientific Research, Bangalore, Jakkur 560064, India; orcid.org/0000-0001-8465-5896; Email: prem@jncasr.ac.in

Authors

Arindam Ghosh – New Chemistry Unit, Bangalore, Jakkur 560064, India; International Centre for Materials Science,

Bangalore, Jakkur 560064, India; School of Advanced Materials, Jawaharlal Nehru Centre for Advanced Scientific Research, Bangalore, Jakkur 560064, India

Dereje Bekele Tekliye – Department of Materials Engineering, Indian Institute of Science, Bengaluru, Karnataka 560012, India

Emily E. Foley – Materials Department, Materials Research Laboratory, University of California Santa Barbara, Santa Barbara, California 93106, United States; orcid.org/0000-0003-2173-7899

Varimalla Raghavendra Reddy – University Campus, UGC-DAE Consortium for Scientific Research, Indore 452001, India

Raphaële J. Clément – Materials Department, Materials Research Laboratory, University of California Santa Barbara, Santa Barbara, California 93106, United States; orcid.org/0000-0002-3611-1162

Gopalakrishnan Sai Gautam – Department of Materials Engineering, Indian Institute of Science, Bengaluru, Karnataka 560012, India; orcid.org/0000-0002-1303-0976

Complete contact information is available at:
<https://pubs.acs.org/10.1021/acs.inorgchem.4c00425>

Notes

The authors declare no competing financial interest.

■ ACKNOWLEDGMENTS

This work was supported by JNCASR. A.G. acknowledges the financial support provided by the DST-INSPIRE research fellowship. G.S.G. acknowledges support from the Science and Engineering Research Board (SERB) of Government of India, under Sanction Numbers SRG/2021/000201 and IPA/2021/000007. The authors also acknowledge the computational resources provided by the Supercomputer Education and Research Centre (SERC), IISc. A portion of the calculations in this work used computational resources of the supercomputer Fugaku provided by RIKEN through the HPCI System Research Project (Project ID hp220393). We acknowledge National Supercomputing Mission (NSM) for providing computing resources of “PARAM Siddhi-AI,” under National PARAM Supercomputing Facility (NPSF), C-DAC, Pune, and being supported by the Ministry of Electronics and Information Technology (MeitY) and Department of Science and Technology (DST), Government of India. The NMR measurements reported here made use of the shared facilities of the Materials Research Science and Engineering Center (MRSEC) at UC Santa Barbara (NSF DMR 2308708). E.E.F. was supported by the NSF Graduate Research Fellowship Program under grant no. DGE 1650114 and was supported by an NSF CAREER award under award no. DMR 2141754. The authors gratefully acknowledge the computing time provided to them on the high-performance computer noctual and noctua2 at the NHR Center PC2. This is funded by the Federal Ministry of Education and Research and the state governments participating on the basis of the resolutions of the GWK for the national high-performance computing at universities (www.nhr-verein.de/unsere-partner). The computations for this research were performed using computing resources under project hpc-prf-emdft.

■ REFERENCES

- (1) Haynes, A. S.; Stoumpos, C. C.; Chen, H.; Chica, D.; Kanatzidis, M. G. Panoramic Synthesis as an Effective Materials Discovery Tool: The System Cs/Sn/P/Se as a Test Case. *J. Am. Chem. Soc.* **2017**, *139* (31), 10814–10821.
- (2) Pienack, N.; Bensch, W. In-Situ Monitoring of the Formation of Crystalline Solids. *Angew. Chem., Int. Ed.* **2011**, *50* (9), 2014–2034.
- (3) Chiring, A.; Mazumder, M.; Pati, S. K.; Johnson, C. S.; Senguttuvan, P. Unraveling the Formation Mechanism of NaCoPO₄ Polymorphs. *J. Solid State Chem.* **2021**, *293* (October 2020), 121766.
- (4) Bianchini, M.; Wang, J.; Clément, R. J.; Ouyang, B.; Xiao, P.; Kitchev, D.; Shi, T.; Zhang, Y.; Wang, Y.; Kim, H.; Zhang, M.; Bai, J.; Wang, F.; Sun, W.; Ceder, G. The Interplay between Thermodynamics and Kinetics in the Solid-State Synthesis of Layered Oxides. *Nat. Mater.* **2020**, *19* (10), 1088–1095.
- (5) Aziz, A.; Carrasco, J. Towards Predictive Synthesis of Inorganic Materials Using Network Science. *Front. Chem.* **2021**, *9* (December), 798838.
- (6) Kim, E.; Huang, K.; Jegelka, S.; Olivetti, E. Virtual Screening of Inorganic Materials Synthesis Parameters with Deep Learning. *Npj Comput. Mater.* **2017**, *3* (1), 53.
- (7) Biradha, K.; Santra, R. Crystal Engineering of Topochemical Solid State Reactionsns. *Chem. Soc. Rev.* **2013**, *42* (3), 950–967.
- (8) Bae, J.; Kim, M.; Kang, H.; Kim, T.; Choi, H.; Kim, B.; Do, H. W.; Shim, W. Kinetic 2D Crystals via Topochemical Approach. *Adv. Mater.* **2021**, *33* (47), 1–35.
- (9) Schaa, R. E.; Mallouk, T. E. Perovskites by Design: A Toolbox of Solid-State Reactions. *Chem. Mater.* **2002**, *14* (4), 1455–1471.
- (10) Ishikawa, H.; Yajima, T.; Miyake, A.; Tokunaga, M.; Matsuo, A.; Kindo, K.; Hiroi, Z. Topochemical Crystal Transformation from a Distorted to a Nearly Perfect Kagome Cuprate. *Chem. Mater.* **2017**, *29* (16), 6719–6725.
- (11) Dey, U. K.; Barman, N.; Ghosh, S.; Sarkar, S.; Peter, S. C.; Senguttuvan, P. Topochemical Bottom-Up Synthesis of 2D- and 3D-Sodium Iron Fluoride Frameworks. *Chem. Mater.* **2019**, *31* (2), 295–299.
- (12) Zhou, X.; Wilfong, B.; Vivanco, H.; Paglione, J.; Brown, C. M.; Rodriguez, E. E. Metastable Layered Cobalt Chalcogenides from Topochemical Deintercalation. *J. Am. Chem. Soc.* **2016**, *138* (50), 16432–16442.
- (13) Lee, K. T.; Ramesh, T. N.; Nan, F.; Botton, G.; Nazar, L. F. Topochemical Synthesis of Sodium Metal Phosphate Olivines for Sodium-Ion Batteries. *Chem. Mater.* **2011**, *23* (16), 3593–3600.
- (14) Smith, A. I.; Wladkowski, H. V.; Hecht, Z. H.; She, Y.; Kattel, S.; Samarawickrama, P. I.; Rich, S. R.; Murphy, J. R.; Tian, J.; Ackerman, J. F.; et al. Alkali Metal Intercalation and Reduction of Layered WO₂Cl₂. *Chem. Mater.* **2020**, *32* (24), 10482–10488.
- (15) Jacobs, J.; Marques, M. A. L.; Wang, H. C.; Dieterich, E.; Ebbinghaus, S. G. Structure, Magnetism, and Thermal Stability of La₂NiO_{2.5}F₃: A Ruddlesden-Popper Oxyfluoride Crystallizing in Space Group P4₂/nnm. *Inorg. Chem.* **2021**, *60* (17), 13646–13657.
- (16) Wissel, K.; Malik, A. M.; Vasala, S.; Plana-Ruiz, S.; Kolb, U.; Slater, P. R.; Da Silva, I.; Alff, L.; Rohrer, J.; Clemens, O. Topochemical Reduction of La₂NiO₃F₂: The First Ni-Based Ruddlesden-Popper $n = 1$ T'-Type Structure and the Impact of Reduction on Magnetic Ordering. *Chem. Mater.* **2020**, *32* (7), 3160–3179.
- (17) Yakubovich, O.; Ursuv, V.; Massa, W.; Frenzen, G.; Babel, D. Zeitschrift Fur Anorganische Und Allgemeine Chemie Structure of Na_xFe_yF_z and Structural Relations in the Family of Weberites. *Z. Anorg. Allg. Chem.* **1993**, *619*, 1909–1919.
- (18) Park, H.; Lee, Y.; Cho, M. K.; Kang, J.; Ko, W.; Jung, Y. H.; Jeon, T. Y.; Hong, J.; Kim, H.; Myung, S. T.; et al. Na₂Fe₂F₇: A Fluoride-Based Cathode for High Power and Long Life Na-Ion Batteries. *Energy Environ. Sci.* **2021**, *14* (3), 1469–1479.
- (19) Foley, E. E.; Wu, V. C.; Jin, W.; Cui, W.; Yoshida, E.; Manche, A.; Clément, R. J. Polymorphism in Weberite Na₂Fe₂F₇ and Its Effects on Electrochemical Properties as a Na-Ion Cathode. *Chem. Mater.* **2023**, *35* (9), 3614–3627.
- (20) Boschloo, G.; Hagfeldt, A. Characteristics of the Iodide/Triiodide Redox Mediator in Dye-Sensitized Solar Cells. *Acc. Chem. Res.* **2009**, *42* (11), 1819–1826.
- (21) Murphy, D. W.; Christian, P. A.; Disalvo, F. J.; Waszczak, J. V. Lithium Incorporation by Vanadium Pentoxide. *Inorg. Chem.* **1979**, *18* (10), 2800–2803.
- (22) Emery, N.; Baddour-Hadjean, R.; Batyrbekuly, D.; Laik, B.; Bakenov, Z.; Pereira-Ramos, J.-P. γ -Na_{0.96}V₂O₅: A New Competitive Cathode Material for Sodium-Ion Batteries Synthesized by a Soft Chemistry Route. *Chem. Mater.* **2018**, *30* (15), 5305–5314.
- (23) Murphy, D. W.; Christian, P. A. Solid State Electrodes for High Energy Batteries. *Science* **1979**, *205* (4407), 651–656.
- (24) Hohenberg, P.; Kohn, W. Inhomogeneous Electron Gas. *Phys. Rev.* **1964**, *136* (3B), B864–B871.
- (25) Kohn, W.; Sham, L. J. Self-Consistent Equations Including Exchange and Correlation Effects. *Phys. Rev.* **1965**, *140* (4A), A1133–A1138.
- (26) Fabbrici, S.; Montanari, E.; Righi, L.; Calestani, G.; Migliori, A. Charge Order and Tilt Modulation in Multiferroic K_xM^{II}_xM^{III}_{1-x}F₃ (0.4 < x < 0.6) Transition Metal Fluorides with Tetragonal Tungsten Bronze Structure. *Chem. Mater.* **2004**, *16* (16), 3007–3019.
- (27) Han, Y.; Hu, J.; Yin, C.; Zhang, Y.; Xie, J.; Yin, D.; Li, C. Iron-Based Fluorides of Tetragonal Tungsten Bronze Structure as Potential Cathodes for Na-Ion Batteries. *J. Mater. Chem. A* **2016**, *4* (19), 7382–7389.
- (28) Ferey, G.; LeBlanc, M.; de Pape, R. Crystal Structure of the Ordered Pyrochlore NH₄Fe^{II}Fe^{III}F₆ Structural Correlations with Fe₂F₅·2H₂O and Its Dehydration Product Fe₂F₅·H₂O. *J. Solid State Chem.* **1981**, *40* (1), 1–7.
- (29) Lemoine, K.; Terry, A.; Hémon-Ribaud, A.; Grenèche, J.-M.; Leblanc, M.; Lhoste, J.; Maisonneuve, V. Contribution of Mössbauer Spectrometry to Structural Characterizations of Iron-Based Fluorinated Materials: Application to Pyrochlore (NH₄)CuFeF₆ and a New Derived Hydrate. *J. Mater. Res.* **2022**, *38* (4), 1138–1148.
- (30) Pironon, J.; Pelletier, M.; De Donato, P.; Mosser-Ruck, R. Characterization of Smectite and Illite by FTIR Spectroscopy of Interlayer NH₄⁺ Cations. *Clay Miner.* **2003**, *38* (2), 201–211.
- (31) Li, C.; Yin, C.; Mu, X.; Maier, J. Top-down Synthesis of Open Framework Fluoride for Lithium and Sodium Batteries. *Chem. Mater.* **2013**, *25* (6), 962–969.
- (32) Hung, I.; Zhou, L.; Pourpoint, F.; Grey, C. P.; Gan, Z. Isotropic High Field NMR Spectra of Li-Ion Battery Materials with Anisotropy > 1 MHz. *J. Am. Chem. Soc.* **2012**, *134* (4), 1898–1901.
- (33) Foley, E. E.; Wong, A.; Vincent, R. C.; Manche, A.; Zaveri, A.; Gonzalez-Correia, E.; Ménard, G.; Clément, R. J. Probing Reaction Processes and Reversibility in Earth-Abundant Na₃FeF₆ for Na-Ion Batteries. *Phys. Chem. Chem. Phys.* **2021**, *23* (36), 20052–20064.
- (34) Burbano, M.; Duttine, M.; Borkiewicz, O.; Wattiaux, A.; Demourgues, A.; Salanne, M.; Groult, H.; Dambournet, D. Anionic Ordering and Thermal Properties of FeF₃·3H₂O. *Inorg. Chem.* **2015**, *54* (19), 9619–9625.
- (35) Férey, G.; Parmentier, J. The Pyrochlore → H.T.B. → ReO₃ Successive Phase Transitions of FeF₃. *Eur. J. Solid State Inorg. Chem.* **1994**, *31*, 697–704.
- (36) de Pape, R.; Tressaud, A.; Portier, J. Sur de Nouvelles Séries de Bronzes Fluores de Composition M_xFeF₃ (M = Na, Rb, Tl). *Mater. Res. Bull.* **1968**, *3* (9), 753–758.
- (37) Tekliye, D. B.; Kumar, A.; Weihang, X.; Mercy, T. D.; Canepa, P.; Sai Gautam, G. Exploration of NaSICON Frameworks as Calcium-Ion Battery Electrodes. *Chem. Mater.* **2022**, *34* (22), 10133–10143.
- (38) Sun, W.; Dacek, S. T.; Ong, S. P.; Hautier, G.; Jain, A.; Richards, W. D.; Gamst, A. C.; Persson, K. A.; Ceder, G. The Thermodynamic Scale of Inorganic Crystalline Metastability. *Sci. Adv.* **2016**, *2* (11), No. e1600225.
- (39) Gocheva, I. D.; Nishijima, M.; Doi, T.; Okada, S.; Yamaki, J.; Nishida, T. Mechanochemical Synthesis of NaMF₃ (M = Fe, Mn, Ni) and Their Electrochemical Properties as Positive Electrode Materials for Sodium Batteries. *J. Power Sources* **2009**, *187* (1), 247–252.

- (40) Dance, J.-M.; Sabatier, R.; Ménil, F.; Wintenberger, M.; Cousseins, J.-C.; Le Flem, G.; Tressaud, A. Etude d'un Nouveau Type de Fluorure Antiferromagnétique à Caractère Bidimensionnel: NaFeF₄. *Solid State Commun.* **1976**, *19* (11), 1059–1065.
- (41) Massiot, D.; Fayon, F.; Capron, M.; King, I.; Le Calvé, S.; Alonso, B.; Durand, J.-O.; Bujoli, B.; Gan, Z.; Hoatson, G. Modelling One- and Two-dimensional Solid-state NMR Spectra. *Magn. Reson. Chem.* **2002**, *40* (1), 70–76.
- (42) Kresse, G.; Hafner, J. Ab Initio Molecular Dynamics for Liquid Metals. *Phys. Rev. B* **1993**, *47* (1), 558–561.
- (43) Kresse, G.; Furthmüller, J. Efficient Iterative Schemes for Ab Initio Total-Energy Calculations Using a Plane-Wave Basis Set. *Phys. Rev. B* **1996**, *54* (16), 11169–11186.
- (44) Joubert, D.; Kresse, G. From Ultrasoft Pseudopotentials to the Projector Augmented-Wave Method. *Phys. Rev. B* **1999**, *59* (3), 1758–1775.
- (45) Hellenbrandt, M. The Inorganic Crystal Structure Database (ICSD)—Present and Future. *Crystallogr. Rev.* **2004**, *10* (1), 17–22.
- (46) Knop, O.; Cameron, T. S.; Jochem, K. What Is the True Space Group of Weberite? *J. Solid State Chem.* **1982**, *43* (2), 213–221.
- (47) Sun, J.; Ruzsinszky, A.; Perdew, J. Strongly Constrained and Appropriately Normed Semilocal Density Functional. *Phys. Rev. Lett.* **2015**, *115* (3), 1–6.
- (48) Sai Gautam, G.; Carter, E. A. Evaluating Transition Metal Oxides within DFT-SCAN and SCAN+U Frameworks for Solar Thermochemical Applications. *Phys. Rev. Mater.* **2018**, *2* (9), 1–14.
- (49) Long, O. Y.; Sai Gautam, G.; Carter, E. A. Evaluating Optimal U for 3d Transition-Metal Oxides within the SCAN+ U Framework. *Phys. Rev. Mater.* **2020**, *4* (4), 1–15.
- (50) Pack, J. D.; Monkhorst, H. J. special Points for Brillouin-Zone Integrations”-a Reply. *Phys. Rev. B* **1977**, *16* (4), 1748–1749.
- (51) Ong, S. P.; Richards, W. D.; Jain, A.; Hautier, G.; Kocher, M.; Cholia, S.; Gunter, D.; Chevrier, V. L.; Persson, K. A.; Ceder, G. Python Materials Genomics (Pymatgen): A Robust, Open-Source Python Library for Materials Analysis. *Comput. Mater. Sci.* **2013**, *68*, 314–319.
- (52) Sai Gautam, G.; Stechel, E. B.; Carter, E. A. Exploring Ca-Ce-M-O (M = 3d Transition Metal) Oxide Perovskites for Solar Thermochemical Applications. *Chem. Mater.* **2020**, *32* (23), 9964–9982.